Meccanica (2022) 57:1125–1138
https://doi.org/10.1007/s11012-022-01480-1

A 3D Griffith peeling model to unify and generalize single and double peeling theories

Daniele Liprandi · Diego Misseroni · Federico Bosia · Massimiliano Fraldi · Nicola M. Pugno

Received: 31 March 2021 / Accepted: 23 December 2021 / Published online: 10 March 2022

Abstract It has been shown in recent years that many species in Nature employ hierarchy and contact splitting as a strategy to enhance the adhesive properties of their attachments. Maximizing the adhesive force is however not the only goal. Many animals can achieve a tunable adhesive force, which allows them to both strongly attach to a surface and easily detach when necessary. Here, we study the adhesive properties of 3D dendritic attachments, which are structures that are widely occurring in nature and which allow to achieve these goals. These structures exploit branching to provide high variability in the geometry, and thus tunability, and contact splitting, to increase the total peeling line and thus the adhesion force. By applying the same principles presented by A.A. Griffith 100 years ago, we derive an analytical model for the detachment forces as a function of their defining angles in 3D space, finding as limit cases 2D double peeling and 1D single peeling. We also develop a numerical model, including a nonlinear elastic constitutive law, for the validation of analytical calculations, allowing additionally to simulate the entire detachment phase, and discuss how geometrical variations influence the adhesive properties of the structure. Finally, we also realize a proof of concept experiment to further validate theoretical/numerical results. Overall, we show how this generalized attachment structure can achieve large variations in its adhesive and mechanical properties, exploiting variations of its geometrical parameters, and thus tunability. The in-depth study of similar basic structural units and their combination can in future lead to a better understanding of the mechanical properties of complex architectures found in Nature.

Keywords Adhesion · Bioinspired · Peeling · Dendritic · Branched

Daniele Liprandi and Diego Misseroni contributed equally.

Supplementary Information The online version contains supplementary material available at https://doi.org/10.1007/s11012-022-01480-1.

D. Liprandi · D. Misseroni · N. M. Pugno (✉)
Laboratory for Bioinspired, Bionic, Nano, Meta Materials & Mechanics, University of Trento, Via Mesiano 77, 38123 Trento, Italy
e-mail: nicola.pugno@unitn.it

F. Bosia
Department of Applied Science and Technology, Politecnico di Torino, Corso Duca degli Abruzzi 24, 10129 Torino, Italy

M. Fraldi
Department of Structures for Engineering and Architecture, University of Napoli "Federico II", Napoli, Italy

N. M. Pugno
School of Engineering and Materials Science, Queen Mary University of London, Mile End Road, London E1 4NS, UK

1 Introduction

Nature provides many examples of biological adhesive surfaces functioning over a wide range of scales and environmental conditions. Natural adhesives often display extraordinary mechanical properties, such as high strength, tunability and self-cleaning. A typical example of such an adhesive structure is a climbing animal toe-pad [1–3]. Adhesive pads exploit van der Waals and/or capillary forces to achieve strong attachment and easy detachment, thus enabling locomotion without an excessive wear of their contact elements [4, 5]. Another interesting case is the spider web attachment disc [6–8]. Depending on the desired functionality, spiders spin their silks in different architectures to form anchorages with varying mechanical properties [7]. Glycoprotein glues are secreted together with the silk to form a fibrous material that adheres to the substrate [8]. Despite the differences between the many examples of adhesives found in Nature, some recurring features can be traced in their geometrical features, in that their structures are often based on the complex organization of fibrils or tape-like elements with sizes that can span across several length scales [9, 10]. In recent years, the mechanical response of these biological structures has been studied in depth, leading to experimental evidence of the correlation between their adhesive properties and their geometries [11–16].

One of the first models used to describe adhesion is Kendall's peeling theory [17] for the detachment of an elastic tape from a rigid substrate. By applying Griffith's criterion [18], presented 100 years ago, adhesive theories for tape-like elements provide an explanation for the presence in biological adhesives of contact splitting, i.e. the procedure of dividing a contact in n sub-contacts to better distribute the load, enhancing the maximal pull-off force by increasing the total width of the peeling front [2, 3]. Moreover, multiple-peeling theory has proven that Kendall's model still holds for complex geometries [19, 20]. This approach has led to many works investigating tape-like hierarchical contacts [1, 21], staple-pin, double tape geometries [7, 22] and conical membranes [23]. Furthermore, studies have been conducting on the effect of different mechanical properties on the peeling forces, i.e. pre-tension [24], bending resistance [25], plasticity [26], viscoelasticity [27], etc. However, when it comes to the description of biological structures, all of these geometries are often considered separately, and each of them is described by a distinct model. This choice is often unrealistic, since many biological adhesive structures have complex geometries which lead to a rich mechanical behaviour that cannot be explained using only one of the afore-mentioned models [12].

In this work, we show how, starting from a single branched element in a generic 3D configuration, we can unify the previous models and obtain highly tunable pull-off forces. The angles determining this simple geometry lead in limit cases to mechanical responses typical of both the single or double peeling theories. We compare the analytical solutions to the results obtained by the numerical model presented in [28], and to those obtained in a proof of concept experiment.

2 Theoretical model

We consider the structure shown in Fig. 1, which can be considered as a basic building block for 3D branched attachments. Two identical tapes are represented as wires, i.e. with negligible width and thickness compared to their length. The tapes are connected at a hinge-like point and form a symmetrical v-shape. Each tape forms an angle θ with the substrate plane. The two tapes form an isosceles triangle of base angle α. The projection of the detached length of the two tapes on the substrate forms an angle 2ϕ. If the attached part is aligned with the detached one, the contact angle becomes equal to ϕ: $\lambda' = \phi$. If a misalignment exists between the two portions, we define a misalignment angle $\lambda = \phi - \lambda'$. An external force is applied to the hinge point at a pull-off angle θ'. The angle α gives rise to a symmetrical structure. In this symmetrical case, it can be demonstrated through energy balance considerations [19, 29] and Griffith [18] theory that the total delamination can be obtained as the composition of two single peeling forces. We first write the peeling force (or, equivalently, pull-off force) of the corresponding single tape peeling problem $\left(\alpha = \frac{\pi}{2}, \theta = \theta', \lambda = 0\right)$, shown in Fig. 1c:

$$F_{SP}(\theta) = wtE\left(\cos\theta - 1 + \sqrt{(1-\cos\theta)^2 + \frac{2\gamma}{Et}}\right) \tag{1}$$

where the subscript SP stands for "Single Peeling", γ is the adhesion energy, E is the tape Young's

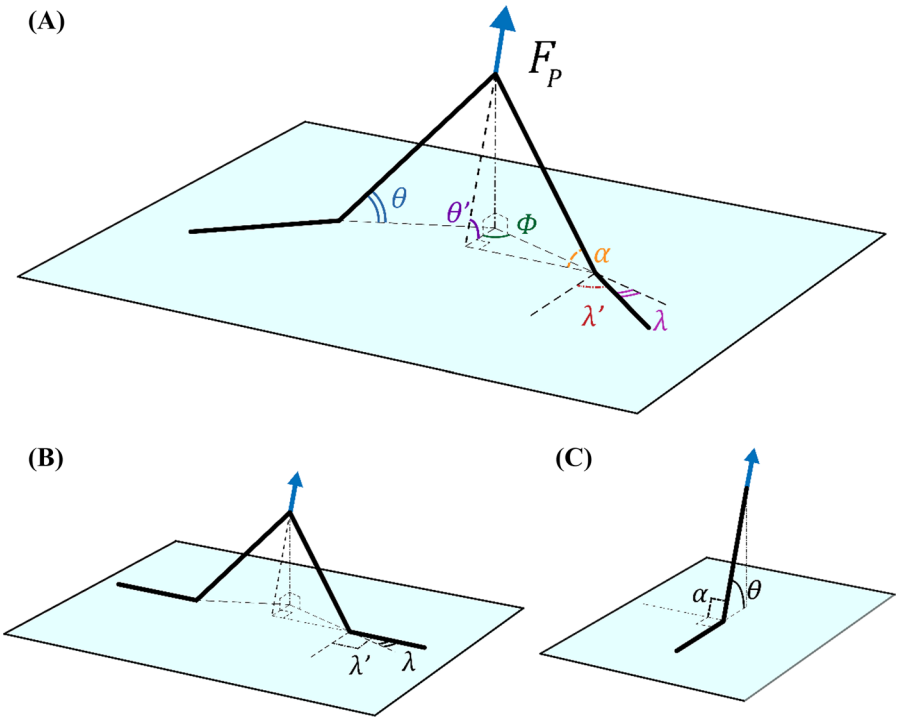

Fig. 1 Schematic representation of the 3D symmetric branched geometry (**a**) and its two limiting cases: **b** double peeling, with $\lambda' = \frac{\pi}{2}$, and **c** single peeling, with $\alpha = \frac{\pi}{2}, \theta' = \theta, \lambda = 0$

modulus, t is its thickness and w its width. We now consider the case for $\alpha \neq \frac{\pi}{2}$. For a v-shaped symmetrical double peeling structure, it is known that the peeling force is [19]

$$F_{DP}(\beta) = 2\sin\beta \cdot wtE\left(\cos\beta - 1 + \sqrt{(1-\cos\beta)^2 + \frac{2\gamma}{Et}}\right) \tag{2}$$

where β is the angle between each tape and the substrate, and the subscript DP stands for "Double Peeling". As shown in Fig. 1a, in a generalized 3D structure, for each branch, the force must be first projected along the tape angle θ and then again along the misalignment angle λ. By applying single tape peeling theory, the critical tape tension at which delamination occurs thus is

$$T_P = wtE\left(\cos\theta\cos\lambda - 1 + \sqrt{(1-\cos\theta\cos\lambda)^2 + \frac{2\gamma}{Et}}\right) \tag{3}$$

where the subscript P stands for "Peeling". Notice that here we are assuming, as done in previous works, that the delamination force is equal to the tension along the tape. In the three-dimensional structure shown in Fig. 1a it can be seen that the two tapes form a triangle of base angle α. We thus sum the two tensions of the tape, as done in [19], to obtain the overall pull-off force. By noticing from Fig. 1a that the angle corresponding to β in Eq. (2) is α, we obtain

$$F_P(\alpha,\theta,\lambda) = 2\sin\alpha \cdot wtE\left(\cos\theta\cos\lambda - 1 + \sqrt{(1-\cos\theta\cos\lambda)^2 + \frac{2\gamma}{Et}}\right) \tag{4}$$

The angles α, ϕ, θ and θ' are not independent. From geometrical considerations, we have the following independent relationships

$$\begin{aligned} \sin\theta &= \sin\alpha \cdot \sin\theta' \\ \cos\alpha &= \cos\theta \cdot \sin\phi \end{aligned} \tag{5}$$

showing that only two angles are needed to uniquely define the structure. Using Eq. (4), we can rewrite Eq. (5) as a function of θ and θ'

$$F_P(\theta',\theta,\lambda) = 2\frac{\sin\theta}{\sin\theta'} \cdot wtE\left(\cos\theta\cos\lambda - 1 + \sqrt{(1-\cos\theta\cos\lambda)^2 + \frac{2\gamma}{Et}}\right) \tag{6}$$

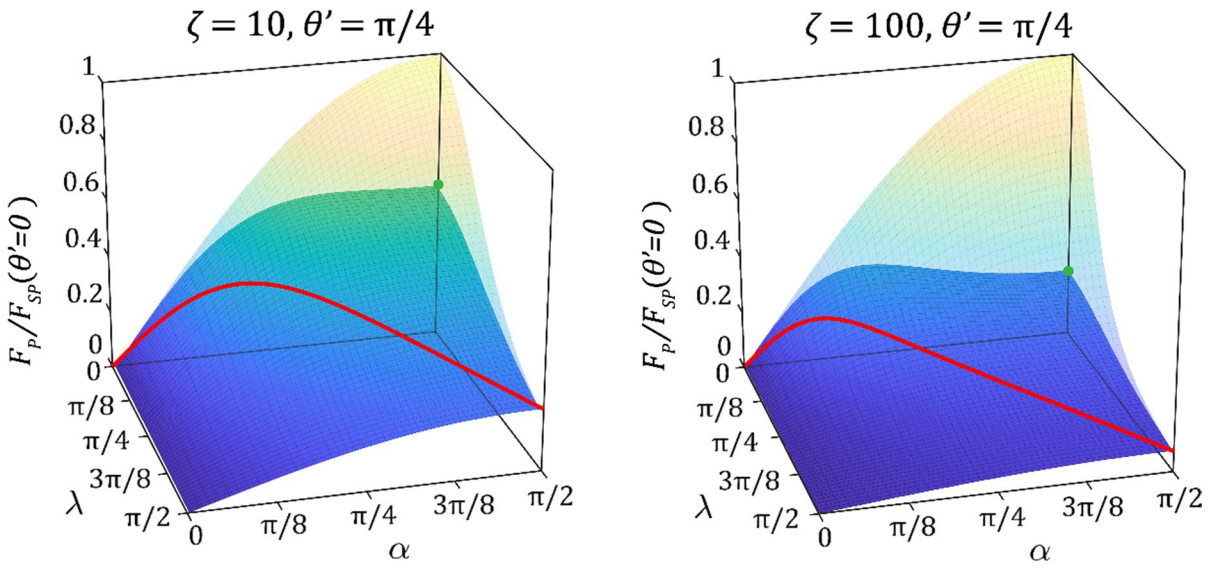

Fig. 2 Normalized peeling force $F_P/F_{SP}(\theta'=0)$ versus α and λ, where $F_P \equiv F_P(\theta'=\pi/4,\zeta;\alpha,\lambda)$, with θ',ζ as fixed parameters and α,λ as variables. The maximal pull-off forces are always reached for $\lambda=0$. The transparent surfaces show the behaviour for $F_P(\theta'=0,\zeta;\alpha,\lambda)/F_{SP}(\theta'=0)$. The green point for $\alpha=\frac{\pi}{2}$ and $\lambda=0$ is the point describing a single peeling problem (Eq. 1), while the red curve describes the behaviour of a double peeling problem (Eq. 2). (Color figure online)

3 Parametric study

From Eq. (4), it is clear that for given tape mechanical properties, the three angles α,θ,λ are the parameters determining the peeling force. We analyse the dependency of the pull-off force by solving Eq. (4) for different values of the coefficient $\zeta = Et/\gamma$, which represents the ratio between elastic and adhesive terms. In this study we consider values of ζ included between 1 and 100. These values can be roughly estimated by the available data in literature concerning biological adhesives [11, 30–32]. Results in Fig. 2 show that a maximum in peeling force is reached for $\lambda=0$, i.e. when attached parts of the tape are aligned with the detaching tape. Both the single tape peeling problem and the symmetrical double peeling problem appear as limiting cases: the single peeling equation for the same pull-off angle θ' occurs for $\alpha=\pi/2,\lambda=0$; the double peeling equation for a splitting angle α is found when $\lambda'=\pi/2$, and thus by applying Eq. (5), the relationship $\cos\theta\cdot\cos\lambda=\cos\alpha$ holds. The latter is represented as a red curve in Fig. 2.

We look at the geometrical constraints to understand the behaviour for $\lim_{\theta'\to 0} F_P(\theta',\theta,\lambda)$. By geometrical construction, we have that $\theta\le\theta'$. This can also be obtained starting from the trigonometrical relations expressed in Eq. (5), which allow us to switch between $F_P(\theta',\theta)$ and $F_P(\theta,\alpha)$ (or any other pair of angles between $\theta,\theta',\alpha,\phi$, describing the detached trait of the tape). We thus obtain that, for $\theta'\to 0$, $\theta\to 0$. To compute the limit, Eq. (4), should therefore be used:

$$\lim_{\theta'\to 0} F_P(\theta',\theta,\lambda) = \lim_{\theta\to 0} F_P(\alpha,\theta,\lambda) = 2\cdot\sin\alpha\cdot wtE\left(\cos\lambda - 1 + \sqrt{(1-\cos\lambda)^2+\frac{2\gamma}{Et}}\right) \quad (7)$$

The effect of the geometrical relations can be better understood by looking at Fig. 3, where the limit scenarios are represented. Notice that in these conditions, α does not depend on θ and θ'. If we recall the double peeling equation, we see that if $\lambda=\alpha$, Eq. (7) is the equation for a symmetrical double peeling case (Fig. 4). If instead $\theta'\to\frac{\pi}{2}$, for geometrical considerations it can be seen that $\alpha\equiv\theta$ and thus we find again Eq. (4).

Finally, we consider the configuration where $\lambda'\in[0,\pi]$, or equivalently $\lambda\in\left[\phi(\theta')-\pi,\phi(\theta')\right]$ (Fig. 5). The curve $\frac{\partial F_P}{\partial\lambda}=0$ corresponds to a misalignment $\lambda=0$, as predicted by Eq. (4). For $\alpha=0$, $\lambda'=\lambda$ and the curve is symmetrical. This is consistent with Eq. (4) which is symmetrical for (θ,λ) since $F_P(\alpha,\theta,\lambda)=F_P(\alpha,\lambda,\theta)$.

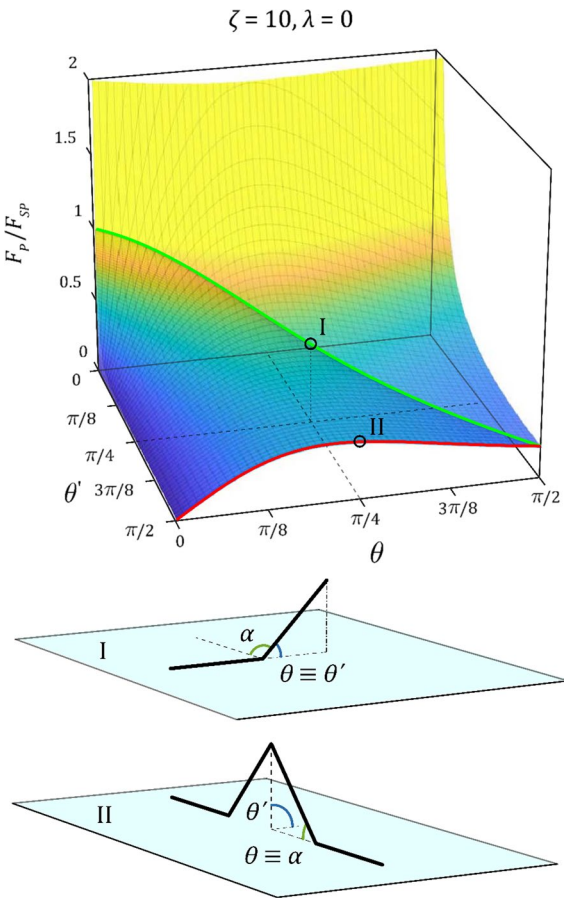

Fig. 3 Normalized peeling force F_P/F_{SP} versus θ' and θ, where $F_P \equiv F_P(\zeta = 10, \lambda = 0; \theta, \theta')$, with ζ, λ as fixed parameters and θ, θ' as variables. The values which satisfy the geometrical relations are highlighted. The green curve $F_P(\lambda, \zeta; \theta, \theta'), \{\theta, \theta' | \alpha = \pi/2\}$ describes the single peeling problem (Eq. 1) while the red curve $F_P(\lambda, \zeta, \theta' = 0; \theta)$ describes the behaviour of the double peeling problem (Eq. 2). The value of α is fixed by Eq. (5). Notice that the maximal pull-off forces are always reached for $\theta' = 0$, as predicted by tape peeling theory. Two limit scenarios are represented: (I) for $\theta = \theta'$ both angles represent the single tape peeling angle, while (II) for $\theta' = \frac{\pi}{2}$, a symmetrical double peeling is created where both α and θ are the governing angles. (Color figure online)

4 Numerical model

We now introduce a numerical model to validate analytical results and to study the evolution of the 3D generalized structure during delamination. In this model, which was introduced in [28, 33], we discretize a tape of negligible width using a set of nodes connected by truss elements of length dL. These one-dimensional elements can have an arbitrary constitutive law, allowing e.g. the simulation of hyperelastic materials. No rotational springs are present in the model; thus, the bending resistance is neglected, since we only consider thin wires/tapes. The adhesion between the tape and the substrate is represented by a 3D fibrillar traction–separation law which is introduced for every node of the tape. The law used in this work is $T = \frac{\mathbf{\Delta} \cdot \psi}{\delta^2} \exp\left(-\frac{\mathbf{\Delta}^2}{\delta^2}\right)$, where T is the exerted traction, $\mathbf{\Delta}$ is the separation, ψ is the adhesive energy per node and δ is the critical length. We assume a monotonically increasing load, leading to crack opening only. A force-control arc-length method is used to simulate the applied force F at an angle θ'. The displacements and internal forces at equilibrium in the structure are calculated using the Newton–Raphson algorithm shown in [28]. During loading, the two branches undergo deformation and delamination, and the angles characterizing the structure change accordingly.

In the following, the chosen geometrical and mechanical characteristics are $L_{det} = 1$ mm, $L_{att} = 2$ mm, $t = 1$ µm, $\theta' = 45°$, where L_{det} and L_{att} are respectively the length of the detached and the attached portions of one branch (these values are chosen arbitrarily, since the peeling force does not depend on them). 800 truss elements are used to describe the 3D structure. We initially study the behaviour of an elastic material, allowing us to compare the numerical results with the theoretical equations. An example of the evolution of the applied force F versus the displacement response u is shown in Fig. 6. The evolution of the two angles θ and ϕ is also shown, together with three dimensional plots which illustrate the behaviour of the structure for different loadings. As shown in Eq. (5), if two of the four angles $\phi, \alpha, \theta, \theta'$ are given then the system is properly defined and the other two angles can be calculated.

As illustrated in [22], if we suppose that δ is infinitesimal, the evolution of the delamination observed in the numerical simulations can be theoretically described using the peeling equations derived from the Griffith energy balance. The tension at which delamination occurs is T_P, given by Eq. (3). Before reaching T_P, the considered tape deforms, and the tension depends exclusively on its elastic properties. We thus indicate this tension as T_{el}:

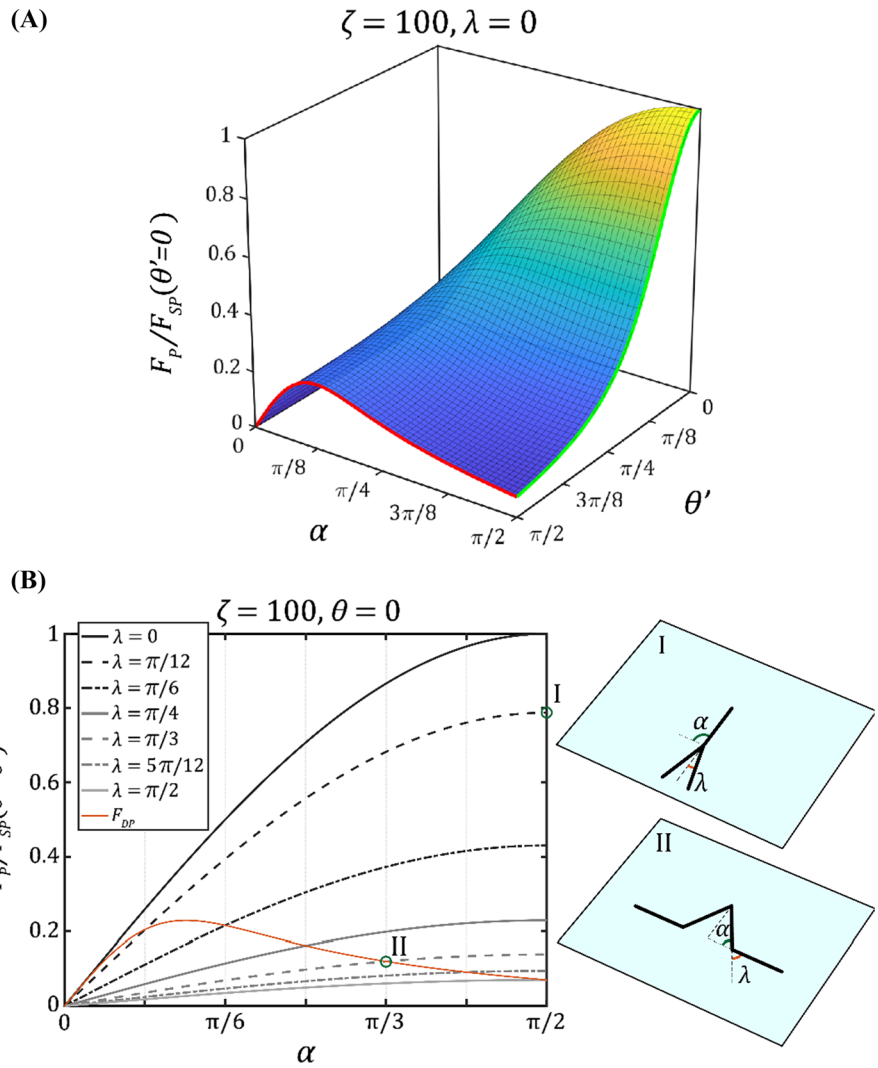

Fig. 4 **a** Normalized peeling force $F_P/F_{SP}(\theta'=0)$ versus θ' and α, where $F_P \equiv F_P(\lambda=0,\zeta=100;\alpha,\theta')$, with λ,ζ as fixed parameters and α,θ' as variables. The green curve $F_P(\lambda,\zeta,\alpha=\pi/2;\theta')$ describes the single peeling Eq. (1) while the red curve $F_P(\lambda,\zeta,\theta'=0;\alpha)$ describes the behaviour of the double peeling equation (Eq. 2). **b** Normalized peeling force $F_P/F_{SP}(\theta'=0)$ versus α for $\theta'=\theta=0$ and different values of the misalignment angle λ. As expected from Eq. (7), for $\alpha=\lambda$ the solution coincides with the double peeling equation. A 3D representation is shown for $\left(\alpha=\frac{\pi}{2},\lambda=\frac{\pi}{12}\right)$ and for $\left(\alpha=\frac{\pi}{3},\lambda=\frac{\pi}{3}\right)$. (Color figure online)

$$T_{el} = wEt\left(\frac{\cos\theta_0}{\cos\theta} - 1\right) \tag{8}$$

where θ_0 is the initial value of θ. We now look at the external load F_{el} during the deformation phase for the 3D generalized structure. F_{el} must consider the superposition of the two peeling processes as already done for Eq. (4):

$$F_{el} = 2\frac{\sin\theta}{\sin\theta'}, T_{el} = 2\frac{\sin\theta}{\sin\theta'}wEt\left(\frac{\cos\theta_0}{\cos\theta} - 1\right) \tag{9}$$

where θ' is assumed to be constant during peeling. Notice that this is true only for $\theta' \neq 0$. For $\theta' = 0$, the expression for F_{el} coincides with the double peeling one provided in [22] for an angle α. We now indicate the applied load at which delamination occurs as $F_P \equiv F_P(\theta,\theta',\lambda)$, with $F_P(\theta,\theta',\lambda)$ given by Eq. (6). When the applied load $F \geq F_P$, delamination begins and the equilibrium path of the structure follows Eq. (6). Notice that an evolution of θ at fixed θ' and λ' leads to an evolution of α and consequentially ϕ and the misalignment λ. The angles and the load continue to evolve until the delamination takes place over the whole finite length of the tapes or when an equilibrium state is reached.

If the initial hypothesis of an infinitesimal critical length δ does not hold, the applied forces measured numerically do not follow the theoretical values previously mentioned. The traction–separation law

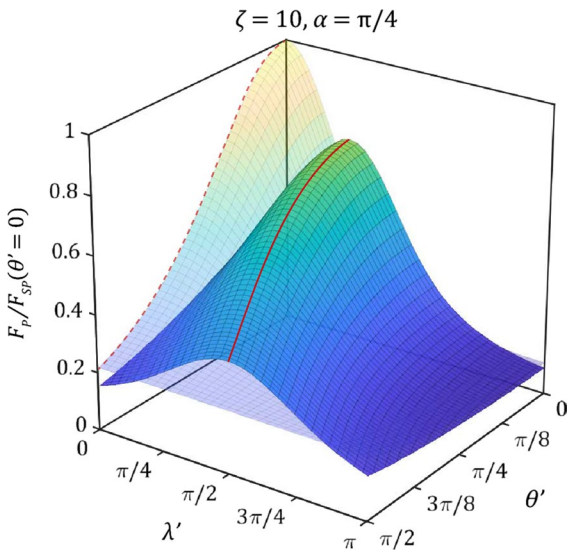

Fig. 5 Normalized peeling force $F_P/F_{SP}(\theta' = 0)$ versus θ' and λ', where $F_P \equiv F_P(\alpha = \pi/4, \zeta = 10; \lambda', \theta')$, with α, ζ as fixed parameters and λ', θ' as variables. $F_P(\alpha = \pi/2, \zeta = 10; \lambda', \theta')/F_{SP}$ is also represented in transparency for comparison. The values of λ' which correspond to $\lambda = 0$ are highlighted by the red line. (Color figure online)

leads to the creation of a cohesive process zone, an area of the substrate where the stresses due to peeling are non-negligible and a curvature of the tape is observed. The dimensions of this area are ruled by the critical length δ. If $\delta \gg dL$, the process zone deforms for $F < F_P$, and thus the equilibrium path becomes smoother, eventually leading to a simultaneous deformation-delamination when the strain distribution at the interface propagates over the entire tape during the elastic phase and thus the expected value of F_P is never reached (Fig. 7).

A difference smaller than 0.01% in the maximal pull-off force between the expected results and the numerical simulation is observed during delamination when all three degrees of freedom are considered (Fig. 8). Further data can be found in the Supplementary Information.

5 Experimental measurements

Quantitative peeling experiments were performed to validate the theoretical and numerical predictions discussed in the previous sections. A transparent elastic tape Tesa® 4204 was used to perform the symmetric double-peeling experiments. The tape has a mean thickness of $t = 52.5 \pm 0.105$ μm and a mean width of $w = 25.39 \pm 0.16$ mm.

5.1 Tensile tests

The mechanical properties of the tape were obtained by 7 preliminary tensile test experiments. These experiments were carried out imposing a constant speed of 0.1 mm/s at one end of the tape with a loading machine (Midi 10, from Messphysik), as shown in Fig. 9a. During the tests, the load was acquired with a DCSRC—1000 N load cell and the displacement with a displacement transducer mounted in the loading frame. The tests were stopped at a strain of about 35%, before the tape failure. An example of a stress–strain curve, representative of the behaviour of all tested samples, is reported in Fig. 9b. The tape's non-linear mechanical behaviour was modelled via a two-segment piecewise linear model, being E_1 and E_2 the slopes of the interpolating lines, representing the two Young's moduli of the tape. The mean values are equal to $E_1 = 1722.61 \pm 165.02$ MPa and $E_2 = 60.96 \pm 3.77$ MPa. The coordinates of the intersection point between the two linear interpolating lines (point A in Fig. 9b) are equal to $\epsilon_1 = 0.0246 \pm 0.003$ and $\sigma_1 = 41.40 \pm 0.99$ MPa.

5.2 Single- peeling tests

The adhesion energy γ was determined performing 10 single-peeling tests using the experimental setup shown in Fig. 9c. In each experiment, 380 mm of tape was peeled from a PMMA rigid substrate (the same used in the double peeling experiments) with a constant speed of 1 mm/s. The experimental setup was specifically designed to align the load cell with the tape axis in the limit peeling condition. This experimental expedient is fundamental so that the load cell works under ideal conditions. Therefore, the load measured by the load cell is exactly the applied force F indicated in Fig. 9c responsible for the delamination of the tape. Load and displacement were acquired with a DBBSM—10 kg load cell and with a displacement transducer mounted in the loading frame, respectively. The experiments were also recorded with a camera (Sony PXW-FS5), positioned laterally to the testing platform, and orthogonal to the tape axis. The camera was synchronized with the data

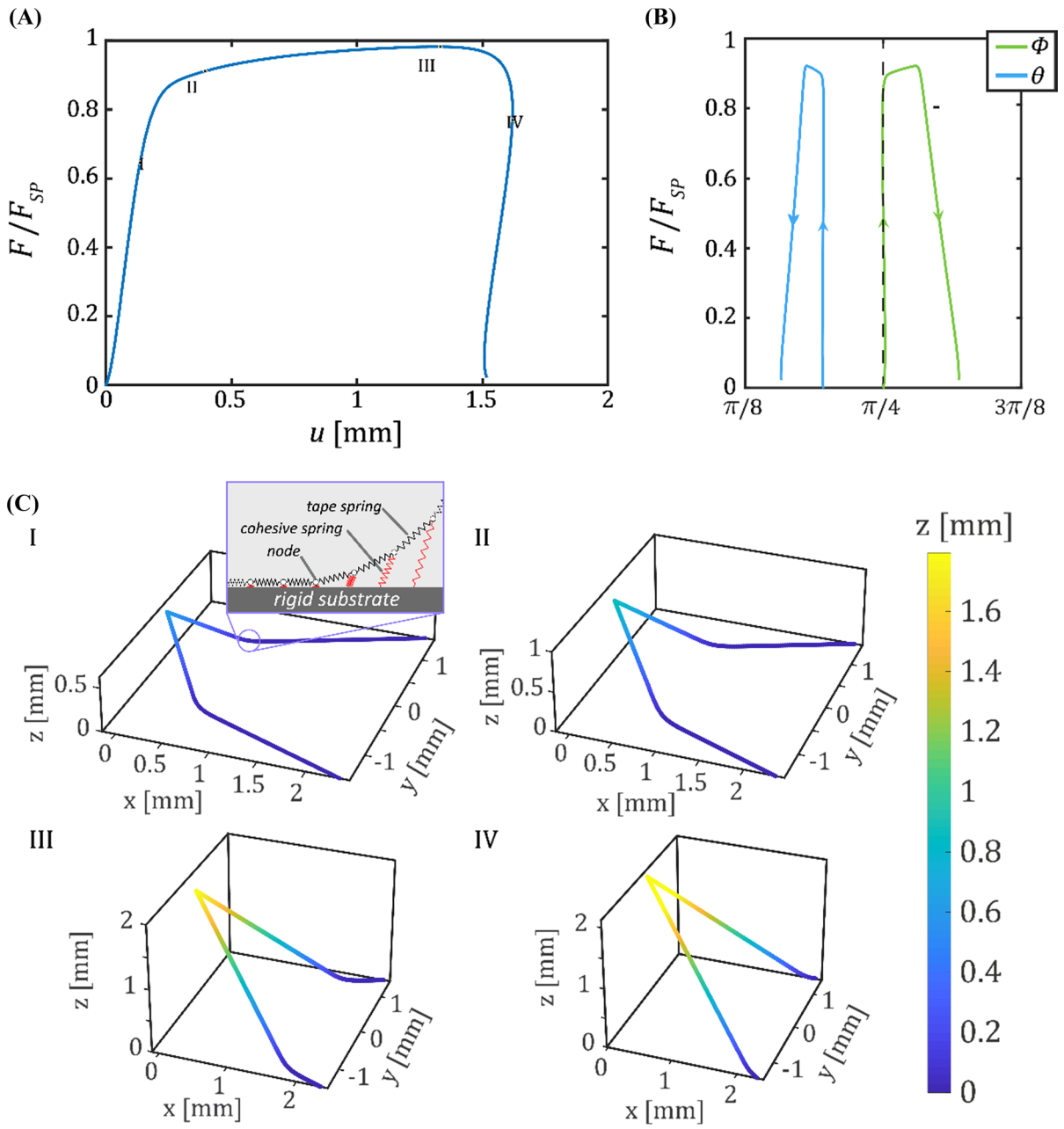

Fig. 6 **a** Normalized applied force $F/F_{SP}(\theta')$ versus displacement for $\theta' = \pi/4$, $\zeta = 10$. The values of α and λ at $F = 0$ are $\alpha = \pi/4$, $\lambda = \pi/8$. **b** Force versus ϕ and θ. The dashed line represents the pull-off angle $\theta' = \pi/4$. Notice that the evolution of ϕ and θ is correlated since θ' is fixed and Eq. (4) must hold. **c** 3-D plots of the structure in four highlighted points: (I) initial deformation and creation of the process zone, (II) beginning of the peeling phase, (III) peak of the force value, (IV) maximal deformation and total delamination. In force-control, after III one should assume the shown curve as the theoretical path, while a sudden failure (i.e. complete delamination) would be observed in an empirical environment. Likewise, in displacement-control the same behaviour should be assumed after IV

acquisition system. Before each test, the PMMA surface was cleaned with a silk cloth dipped in ethanol and the tape was pressed on the PMMA surface with a metal roller coated with a thin (thickness 2 mm) rubber layer to guarantee the same initial condition. Since the test is done in a single peeling

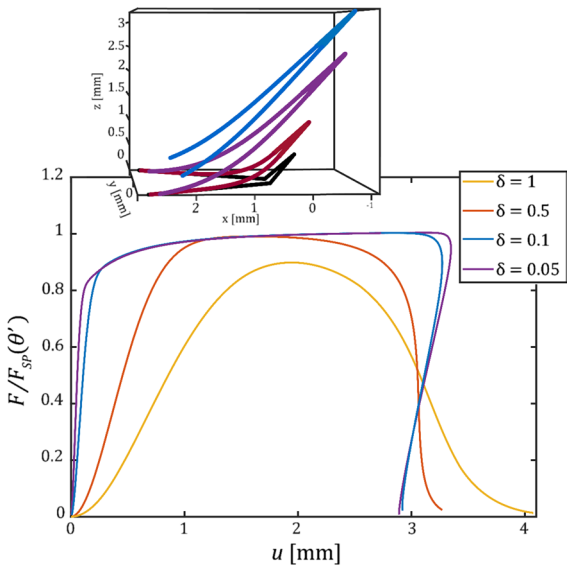

Fig. 7 Normalized applied force $F/F_{SP}(\theta')$ versus displacement for different values of the process zone critical length δ (in mm) and for an attached length $L_{att} = 4$ mm and a discretization step of $dL = 0.01$ mm. For $\delta = 1$ mm, the deformation and delamination phases are indiscernible. This happens because the strain field reaches the end of the tape before the process zone reaches its regime. Thus, $F < F_P$ during the whole deformation

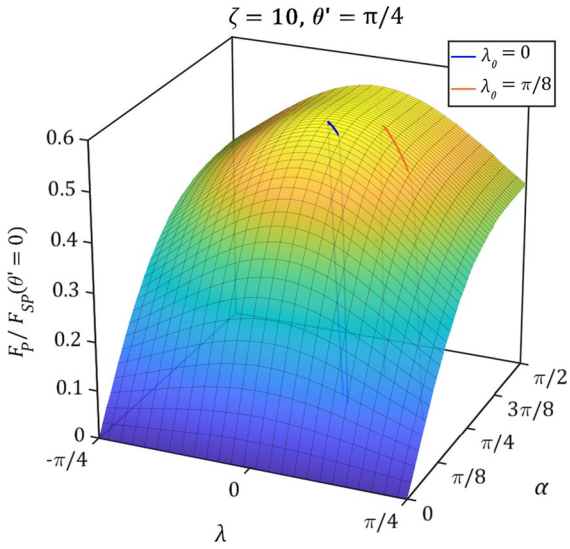

Fig. 8 Normalized peeling force $F_P/F_{SP}(\theta' = 0)$ versus λ and α, where $F_P \equiv F_P\left(\theta' = \frac{\pi}{4}, \zeta = 10; \lambda, \alpha\right)$, with θ', ζ as fixed parameters and λ, α as variables. Two numerical solutions which differ for the initial value λ_0 are superimposed onto the analytical result. There is a very good agreement between analytical and numerical results during the delamination phase, with a maximal difference smaller than the 0.01%

configuration, we assume that the force measured during detachment equals the predicted critical pull-off force F_{SP}, expressed in Eq. (1). For every experiment, the mean critical pull-off force $F_{SP\,\mathrm{exp}}$ required to peel the tape from the PMMA substrate was assumed to be equal to the horizontal fitting line (black/dashed line in the figure) evaluated between 25 and 100 mm (white range in the figure), after the limit peeling condition ($\theta' = \theta'_{lim}$) is reached. By averaging such forces $F_{SP\,\mathrm{exp}}$, estimated for each of the 10 tests, we determined a mean critical pull-off force $\overline{F_{SP_{exp}}} = 54.30 \pm 0.95$ N. The experimental results obtained from the 10 tests, namely the applied force F as a function of the vertical displacement, are summarized in Fig. 9d. In the figure, the magenta/continuous thick line and the magenta vertical thin lines represent, respectively, the average applied force and the standard deviation computed at all times considering all the experiments. Knowing the critical peeling force $\overline{F_{SP_{exp}}}$ required to peel the tape from the substrate, we calculated the corresponding adhesion energy γ through Eq. (1), obtaining

$$\gamma = \frac{\overline{F_{SP_{exp}}}}{w}\left(1 - \cos\theta'_{lim}\right) + \frac{\overline{F_{SP_{exp}}}^2}{2E_1 t w^2} \tag{10}$$

where θ'_{lim} is the limit peeling angle. This angle was estimated equal to 0.319 ± 0.007 rad exploiting the results of the 10 experiments. In Eq. (10), the second term on the right side considers the extensibility of the tape. Since the applied force is small, it is reasonable to consider in such expression the Young Modulus equal to E_1. A mean value of $\gamma = 133.42 \pm 2.77$ J/m^2 was estimated for the adhesion energy.

5.3 3D peeling tests

An ad hoc experimental setup, shown in Fig. 10a, was conceived and realized to perform the 3D peeling experiments. The experiments were conducted by peeling the adhesive tape from a rigid PMMA substrate for two different values of the contact angle λ'. In one case, we imposed $\lambda' = \pi/9$, in the other $\lambda' = 2\pi/9$. For each angle we performed 16 experiments. At the beginning of each test, the same protocol used for the single peeling experiments was used, again to guarantee the same initial conditions in every test. The rigid PMMA substrate of length

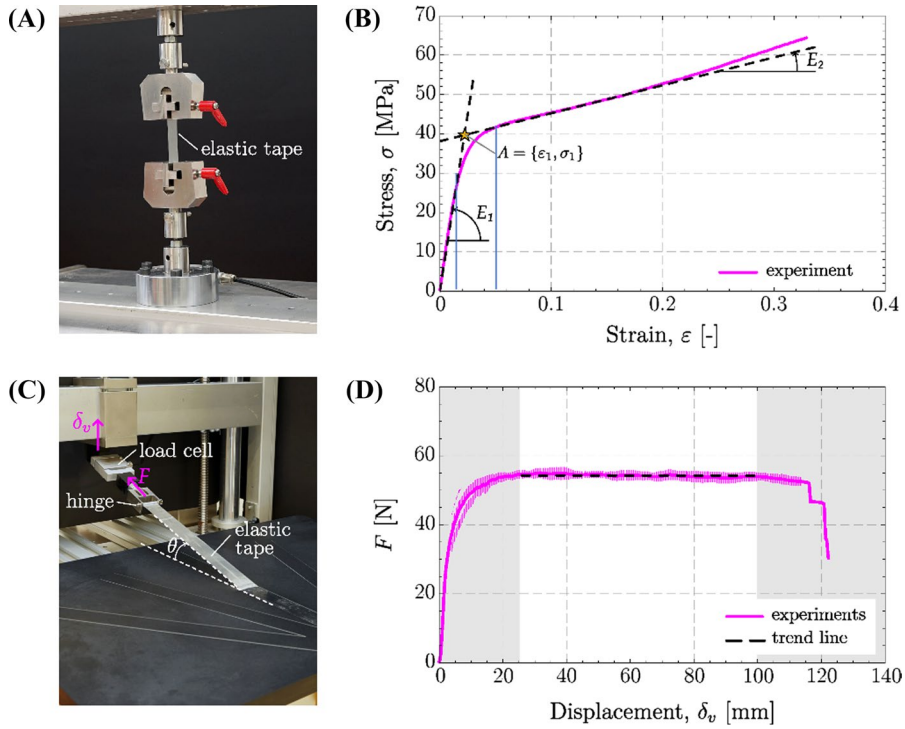

Fig. 9 **a** Setup exploited to perform the tensile tests on the adhesive transparent tape and **b** an example of a stress–strain curve, representative of the general trend of all tested samples. **c** Setup used to perform the single peeling tests and **d** the experimental results reported in terms of applied force-vertical displacement. The vertical displacement–time rate was 1 mm/s. The magenta/continuous thick line and the thin vertical lines represent, respectively, the average applied force and the standard deviation computed, at all times, considering all the recorded data of the 10 tests. The horizontal fitting line (black/dashed line) represents the average critical peeling force $\overline{F_{SP_{exp}}}$ evaluated between 25 and 100 mm, namely the white range in the figure. (Color figure online)

600 mm and width 400 mm was engraved with a 45° conical tool mounted on a milling machine (EGX-600 from Roland, resolution 0.01 mm), as highlighted in Fig. 10a. This machining is fundamental to allow the exact alignment of the tape at the beginning of each experiment for the two investigated cases. Two different PMMA self-aligning mechanisms (one for $\lambda' = \pi/9$, in the other $\lambda' = 2\pi/9$) were specifically designed to couple the tape to a miniaturized load cell and to the loading frame machine. The detail of this mechanism is shown in the inset of Fig. 10a.

Four snapshots taken during the execution of one test showing the working principle of the self-aligning mechanism are reported in Fig. 10b. In each experiment, 400 mm of tape was peeled from the PMMA rigid substrate by imposing a constant vertical speed of 1 mm/s to the self-aligning mechanism with a loading frame machine (MIDI 10). During the experiment, the applied force F was measured with the miniaturized load cell (XFTC-300, R.C. 200 N) mounted on the pendular mechanism and the vertical displacement with a displacement transducer mounted on the loading frame machine. To capture the variation of the pull-off angle θ' and the angle between the tape and the substrate α, the experiments were also recorded with two cameras (Sony PXW-FS5 and PXW-FS7), positioned orthogonally to the testing platform, one frontally and the other laterally, as sketched in Fig. 10c. Figure 10d shows the superposition of two snapshots taken at the same time with the two synchronized cameras. By exploiting the principles of orthogonal projections, it is possible to determine the pull-off angle θ' directly and the angle α by a simple trigonometric relation. The two cameras were triggered with a NI CompactRIO system interfaced with LabView 2020 (National Instruments)

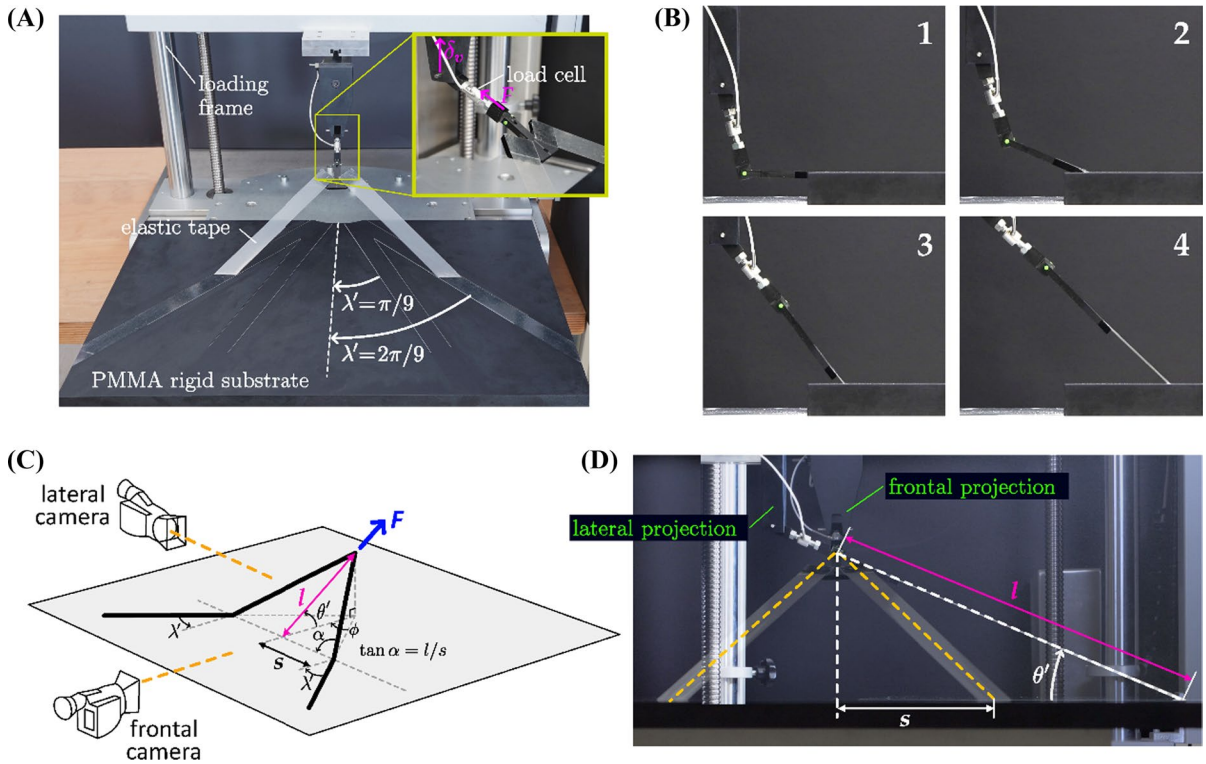

Fig. 10 **a** Experimental setup designed to perform the double peeling experiments. **b** Frame sequence illustrating the working principle of the self-aligning mechanism conceived to connect the tape to the miniaturized load cell and the loading frame. **c** Sketch showing the position of the two cameras used to capture the variation of the pull-off angle θ' and the angle between the tape and the substrate α. **d** Superposition of two snapshots taken with the two cameras. By using the principles of orthogonal projections, we estimated the pull-off angle θ' and the angle α via a simple trigonometric relation

to be synchronized with the loading frame and the load cell acquisition.

6 Comparison between theory, simulations and experiments

The experimental values are compared to numerical results obtained with the described numerical model. The constitutive law for the tape material used in the model is

$$\sigma = \begin{cases} E_1\varepsilon & \varepsilon < \varepsilon_1 \\ E_1\varepsilon_1 + E_2(\varepsilon - \varepsilon_1) & \varepsilon \geq \varepsilon_1 \end{cases} \tag{11}$$

where E_1, E_2 and ε_1 are those obtained experimentally. To correctly simulate the experimental setup, the displacement is imposed at the tip of a rigid tape length of 64.0 mm with $E_{load} = 10^5 E_1$, representing the load cell. Two segments with the same Young's modulus are connected to the load cell to simulate the PMMA auto-aligning mechanisms. Simulations were carried out using the experimentally derived adhesive energy value of $\gamma = 133.42$ J/m^2 and a cohesive critical length of $\delta = 2$ mm. To convert the adhesive energy γ to the adhesive energy per node ψ, we associate with every node an area $dL \cdot w$, where dL is the length of each element of the numerical model and w is the width of the tape, measured experimentally.

The comparison between theory, numerical and experimental results are shown in Fig. 11. The evolution over time of the applied force per unit width of the tape are reported in Fig. 11a for a contact angle $\lambda' = \pi/9$ and, in Fig. 11b for $\lambda' = 2\pi/9$. The yellow triangles represent the peeling force predicted theoretically, the blue dots represent the numerical results

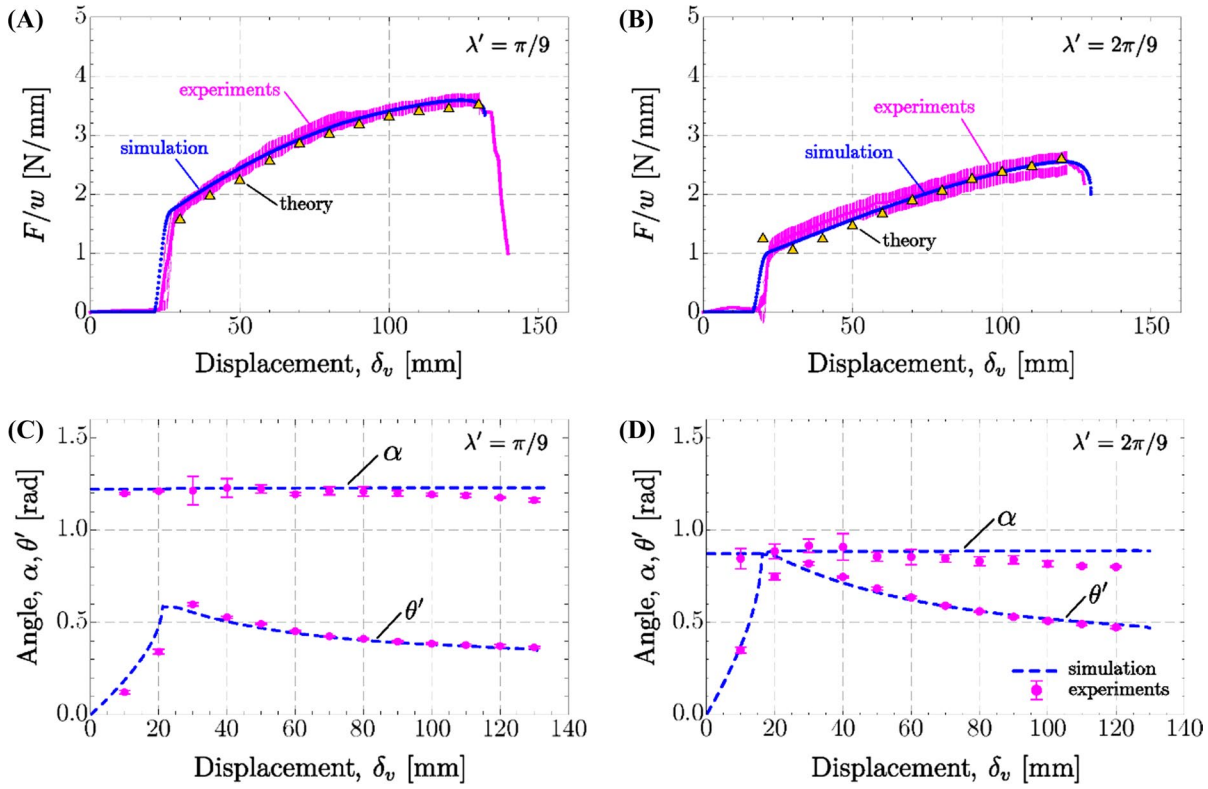

Fig. 11 Comparison between theoretical, numerical, and experimental results. **a** Force per tape width for $\lambda' = \pi/9$. **b** Force per tape width for $\lambda' = 2\pi/9$. The yellow/triangles markers represent the pull-off force calculated from Eq. (4) considering the experimental value of the angles θ' and α reported in subfigures below, the blue/dots the numerical predictions and the magenta lines the experimental results. **c** θ' and α values for $\phi = \lambda' = \pi/9$. **d** θ' and α values for $\phi = \lambda' = 2\pi/9$. The magenta/disks and their relative bars represent, respectively, the mean value and the standard deviation of experimental values of the angles θ' and α, while the blue/dashed lines refer to the numerical results. (Color figure online)

and, the magenta lines the experimental results. The magenta continuous thick line and the magenta vertical thin lines represent, respectively, the average applied force and the standard deviation computed, at all times, considering all the experiments. The theoretical values of the peeling force are computed by Eq. (4), considering the experimental value of the angles θ' and α reported in Fig. 11c, d. The numerical results are obtained using the numerical model described in Sect 4. In the model, we have considered the same geometry of the setup and the same mechanical properties of the tape to mimic the real experiments. Starting from $\theta' = 0$, the auto-aligning mechanism attached to the load cell (inset of Fig. 10a and b) rotates until deformation begins ($t \approx 20$ s) causing a rapid increase of the applied force until the mechanism reaches an almost steady inclination. From this moment on, the applied force continues to grow, but with a lower slope, up to the complete detachment of the tape from the substrate ($t \approx 140$ s for $\lambda' = \pi/9$ and $t \approx 130$ $\lambda' = 2\pi/9$). By studying the strain evolution in the tape, it can be seen that its value is constantly lower than the critical value ε_1 (see Supplementary Information, Figure S.IV). The figures clearly show the very good agreement between the theory and both numerical and experimental results.

Figure 11c and d show the evolution over time of the angles θ' and α for the two cases $\lambda' = \pi/9$ and $\lambda' = 2\pi/9$, respectively, and their comparison with those predicted by the numerical model. In these figures, the magenta/disks and their relative bars represent, respectively, the mean value and the standard deviation of experimental values of the angles θ' and α, while the blue/dashed lines refer to

the numerical results. To estimate the values of such angles, a specific algorithm was developed in Mathematica to perform an image-correlation analysis on the frames recorded by the two cameras (see Fig. 11) at 10-s interval. During the evolution of the experiments, the angle α between the tape and the substrate remains almost constant, as correctly predicted by the numerical model. On the contrary, the pull-off angle θ' shows, accordingly with the results reported in Fig. 11a and b, a rapid increase until deformation begins ($t \approx 20$ s), and then tends to decrease. Observing the figures, it is evident that the numerical model captures the behaviour observed in the experiments very well, and can therefore correctly reproduce the different phases of delamination.

7 Conclusions

We have studied the adhesive properties of a doubly branched 3D generalized structure made of tape-like attachments and shown how the different angles forming the geometry influence the peeling force. We have shown that the 3D structure admits as limiting cases single tape peeling and symmetrical double peeling, and we have derived the corresponding behaviour, proving that both can be described by a single general equation. By using a numerical method based on a finite element analysis, we have confirmed the validity of the analytical solution, and also described the evolution of dendritic two-branched structures during delamination, which give rise to a richer phenomenology than that of single tape peeling or a symmetrical double peeling, since two additional degrees of freedom are introduced. Finally, experimental tests were performed to validate the theoretical/numerical results. The proposed formalism could help biologists better understand the adhesive behaviour of natural structures, generalizing basic geometries such as single or double tape contacts, and to further study the role of geometry in determining tunability of the adhesive force achieved by animals and plants.

Funding FB, DM and NMP are supported by the European Commission under the H2020 FET Open ("Boheme") Grant No. 863179. This work was carried out within the COST Action CA15216 "European Network of Bioadhesion Expertise: Fundamental Knowledge to Inspire Advanced Bonding Technologies". NMP and MF are also supported by the Italian Ministry of Education, University and Research (MIUR) under the PRIN-20177TTP3S grant.

Declarations

Conflict of interest The authors declare that they have no conflict of interest.

References

1. Autumn K, Liang YA, Hsieh ST, Zesch W, Chan WP, Kenny TW, Fearing R, Full RJ (2000) Adhesive force of a single gecko foot-hair. Nature 405:681–685. https://doi.org/10.1038/35015073
2. Arzt E, Gorb SN, Spolenak R (2003) From micro to nano contacts in biological attachment devices. Proc Natl Acad Sci 100:10603–10606. https://doi.org/10.1073/pnas.1534701100
3. Varenberg M, Pugno NM, Gorb SN (2010) Spatulate structures in biological fibrillar adhesion. Soft Matter 6:3269. https://doi.org/10.1039/c003207g
4. Autumn K et al (2002) Evidence for van der Waals adhesion in gecko setae. Proc Natl Acad Sci 99:12252–12256. https://doi.org/10.1073/PNAS.192252799
5. Huber G, Mantz H, Spolenak R, Mecke K, Jacobs K, Gorb SN, Arzt E (2005) Evidence for capillarity contributions to gecko adhesion from single spatula nanomechanical measurements. Proc Natl Acad Sci 102:16293–16296. https://doi.org/10.1073/PNAS.0506328102
6. Sahni V, Blackledge TA, Dhinojwala A (2011) A review on spider silk adhesion. J Adhes 87:595–614. https://doi.org/10.1080/00218464.2011.583588
7. Sahni V, Harris J, Blackledge TA, Dhinojwala A (2012) Cobweb-weaving spiders produce different attachment discs for locomotion and prey capture. Nat Commun 3:1106–1107. https://doi.org/10.1038/ncomms2099
8. Wolff JO, Gorb SN (2016) Attachment structures and adhesive secretions in arachnids. Springer International Publishing, Cham
9. Wolff JO, Grawe I, Wirth M, Karstedt A, Gorb SN (2015) Spider's super-glue: thread anchors are composite adhesives with synergistic hierarchical organization. Soft Matter 11:2394–2403. https://doi.org/10.1039/c4sm02130d

10. Chen B, Wu P, Gao H (2008) Hierarchical modelling of attachment and detachment mechanisms of gecko toe adhesion. Proc R Soc A Math Phys Eng Sci 464:1639–1652. https://doi.org/10.1098/rspa.2007.0350
11. Gravish N, Wilkinson M, Autumn K (2008) Frictional and elastic energy in gecko adhesive detachment. J R Soc Interface 5:339–348. https://doi.org/10.1098/rsif.2007.1077
12. Wolff JO, Herberstein ME (2017) Three-dimensional printing spiders: Back-and-forth glue application yields silk anchorages with high pull-off resistance under varying loading situations. J R Soc Interface. https://doi.org/10.1098/rsif.2016.0783
13. Meng F, Liu Q, Wang X, Tan D, Xue L, Jon P, Barnes W (2019) Tree frog adhesion biomimetics: opportunities for the development of new, smart adhesives that adhere under wet conditions. Philos Trans R Soc A Math Phys Eng Sci. https://doi.org/10.1098/rsta.2019.0131
14. Wolff JO et al (2019) Evolution of aerial spider webs coincided with repeated structural optimization of silk anchorages. Evolution 73:2122–2134. https://doi.org/10.1111/evo.13834
15. Greco G, Pantano MF, Mazzolai B, Pugno NM (2019) Imaging and mechanical characterization of different junctions in spider orb webs. Sci Rep. https://doi.org/10.1038/s41598-019-42070-8
16. Greco G, Wolff JO, Pugno NM (2020) Strong and tough silk for resilient attachment discs: the mechanical properties of piriform silk in the spider cupiennius salei (Keyserling, 1877). Front Mater. https://doi.org/10.3389/fmats.2020.00138
17. Kendall K (1975) Thin-film peeling-the elastic term. J Phys D Appl Phys 8:1449–1452. https://doi.org/10.1088/0022-3727/8/13/005
18. Griffith AA (1921) The phenomena of rupture and flow in solids. Philos Trans R Soc Lond Ser A Contain Pap Math Phys Charact 221:163–198. https://doi.org/10.1098/rsta.1921.0006
19. Pugno NM (2011) The theory of multiple peeling. Int J Fract 171:185–193. https://doi.org/10.1007/s10704-011-9638-2
20. Brely L, Bosia F, Pugno NM (2014) Numerical implementation of multiple peeling theory and its application to spider web anchorages. Interface Focus 5:1–9. https://doi.org/10.1098/rsfs.2014.0051
21. Bhushan B (2007) Adhesion of multi-level hierarchical attachment systems in Gecko feet. J Adhes Sci Technol 21:1213–1258. https://doi.org/10.1163/156856107782328353
22. Brely L, Bosia F, Palumbo S, Fraldi M, Dhinojwala A, Pugno NM (2019) Competition between delamination and tearing in multiple peeling problems. J R Soc Interface 16:20190388. https://doi.org/10.1098/rsif.2019.0388
23. Afferrante L, Carbone G, Demelio G, Pugno NM (2013) Adhesion of elastic thin films: double peeling of tapes versus axisymmetric peeling of membranes. Tribol Lett 52:439–447. https://doi.org/10.1007/s11249-013-0227-6
24. Chen B, Wu P, Gao H (2009) Pre-tension generates strongly reversible adhesion of a spatula pad on substrate. J R Soc Interface 6:529–537. https://doi.org/10.1098/rsif.2008.0322
25. Sauer RA (2011) The peeling behavior of thin films with finite bending stiffness and the implications on gecko adhesion. J Adhes 87:624–643. https://doi.org/10.1080/00218464.2011.596084
26. Wei Y, Hutchinson JW (1998) Interface strength, work of adhesion and plasticity in the peel test. Int J Fract 93:315–333. https://doi.org/10.1007/978-94-017-2854-6_16
27. Peng Z, Wang C, Chen L, Chen S (2014) Peeling behavior of a viscoelastic thin-film on a rigid substrate. Int J Solids Struct 51:4596–4603. https://doi.org/10.1016/j.ijsolstr.2014.10.011
28. Liprandi D, Bosia F, Pugno NM (2019) A theoretical-numerical model for the peeling of elastic membranes. J Mech Phys Solids. https://doi.org/10.1016/j.jmps.2019.103733
29. Gent AN, Kaang S (1986) Pull-off forces for adhesive tapes. J Appl Polym Sci 32:4689–4700. https://doi.org/10.1002/app.1986.070320433
30. Labonte D, Federle W (2016) Biomechanics of shear-sensitive adhesion in climbing animals: peeling, pre-tension and sliding-induced changes in interface strength. J R Soc Interface. https://doi.org/10.1098/rsif.2016.0373
31. Autumn K, Dittmore A, Santos D, Spenko M, Cutkosky M (2006) Frictional adhesion: a new angle on gecko attachment. J Exp Biol 209:3569–3579. https://doi.org/10.1242/jeb.02486
32. Drotlef DM, Appel E, Peisker H, Dening K, del Campo A, Gorb SN, Barnes WJP (2014) Morphological studies of the toe pads of the rock frog, staurois parvus (family: Ranidae) and their relevance to the development of new biomimetically inspired reversible adhesives. Interface Focus 5:1–11. https://doi.org/10.1098/rsfs.2014.0036
33. Brely L, Bosia F, Pugno NM (2018) The influence of substrate roughness, patterning, curvature, and compliance in peeling problems. Bioinspir Biomim 13:026004. https://doi.org/10.1088/1748-3190/aaa0e5

For the centenary of the Griffith theory: A 3D Griffith peeling model to generalize single and double peeling theories

Supplementary materials

Daniele Liprandi[1,=], Diego Misseroni[1,=], Federico Bosia[2], Massimiliano Fraldi[3], Nicola M. Pugno[1,4*]

[1] Laboratory for Bioinspired, Bionic, Nano, Meta Materials & Mechanics, University of Trento, Via Mesiano 77, I-38123 Trento, Italy

[2] Department of Applied Science and Technology, Politecnico di Torino, Corso Duca degli Abruzzi 24, 10129 Torino, Italy

[3] Department of Structures for Engineering and Architecture, University of Napoli "Federico II", Italy

[4] School of Engineering and Materials Science, Queen Mary University of London, Mile End Road, London E1 4NS, United Kingdom

[=] These authors contributed equally.

*nicola.pugno@unitn.it

Tape peeling equation

We consider an infinite elastic tape of Young's modulus E, width w, thickness t. The tape adheres to a rigid substrate. When the detachment of a length Δl occurs, the Griffith criterion relative to the creation of a new surface $A = w \cdot \Delta l$ gives us:

$$\frac{\partial \Pi}{\partial A} = \frac{\partial (U_e - W + U_s)}{\partial A} < 0 \tag{S1}$$

where W is the work associated to the external applied force F, U_e is the elastic energy and U_s is the surface (i.e. adhesive) energy. The surface energy can be expressed as

$$U_s = A\gamma \tag{S2}$$

With γ being the adhesive energy per unit area, i.e the energy contribution required for the creation of a new surface of unit area.

In the case of a tape with constant width w, substituting Eq. (S2), Eq. (S1) becomes:

$$\frac{\partial W}{\partial A} - \frac{\partial U_e}{\partial A} > w\gamma \tag{S3}$$

The variation of work for an angle θ between the external load and the substrate is:

$$\frac{\partial W}{\partial A} = F(1 - \cos\theta) + \frac{F^2}{wtE} \tag{S4}$$

where the second term derives from the work done in stretching the tape. The elastic energy U_e is given by the axial stress and strain of the tape.

$$\frac{\partial U_e}{\partial A} = \frac{1}{2} wtE\epsilon^2 = \frac{1}{2}\frac{F^2}{wtE} \tag{S5}$$

where ε is the strain of the tape, and the relationship $F = \epsilon E \cdot wt$ is used to explicitly include the external force. Substituting S4 and S5 in S3 gives:

$$F\ (1 - \cos\theta) + \frac{F^2}{2wtE} > w\gamma \tag{S6}$$

Solving for F gives the analytical expression for the peeling force:

$$F > F_{SP} = Ewt\left[cos(\theta) - 1 + \sqrt{\left(1 - cos(\theta)\right)^2 + \frac{2\gamma}{tE}}\right] \tag{S7}$$

Where we've indicated with F_{SP} the force critical value.

λ' variations and dissipated energy

Adhesive pull-off forces and dissipated energies are affected by angle variations. Here, we show the peeling evolution for structures with different angles λ' (See Figure 1 in the main manuscript). After total delamination, the elastic energy stored in the structure is released. This is visible in Figure S.I, where for a single curve we have indicated the two dissipated energies U_{del} and U_{el}, which are the energy released by the adhesive interface and the energy released by the elastic deformation respectively. The snapback effect corresponds to the relaxation occurring in the stretched tape once total delamination begins. We are able to observe this behaviour because we use an arc-length method, which follows the theoretical path of the peeling problem.

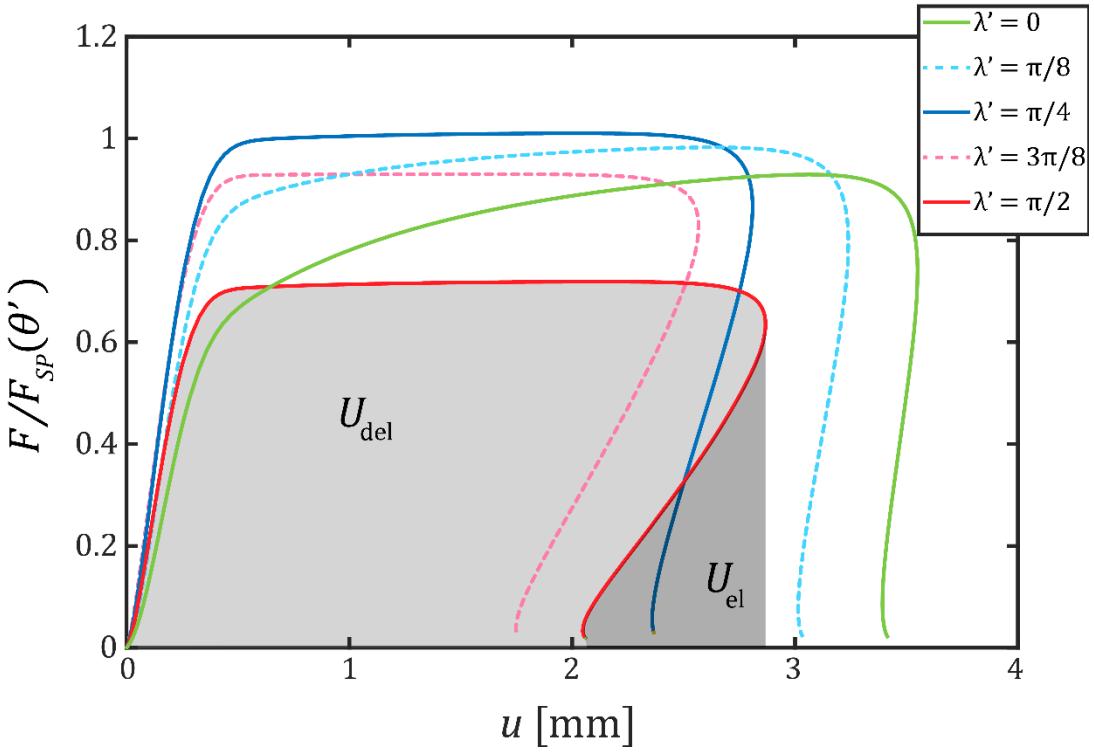

Figure S.I Normalized external force $F/F_{SP}(\theta')$ vs displacement for different values of λ' for $\theta' = \pi/4$, $\phi = \pi/4$. The maximal force is reached for $\lambda' = \phi$. The adhesive and elastic energy contributions are reported for $\lambda = \frac{\pi}{2}$, i.e. the double peeling configuration.

Misalignment and force evolution

The effect of the misalignment given by ϕ and λ can be better observed in Figure S.II, where the evolution of α is shown for different values of α_0 at fixed λ_0. Notice that in a double peeling structure with an initial angle $\theta_0 = 0$ the equilibrium state coincides with the first delamination state. This is not true in our case since, even for $\alpha_0 = 0$, there still is an evolution of α after the first delamination.

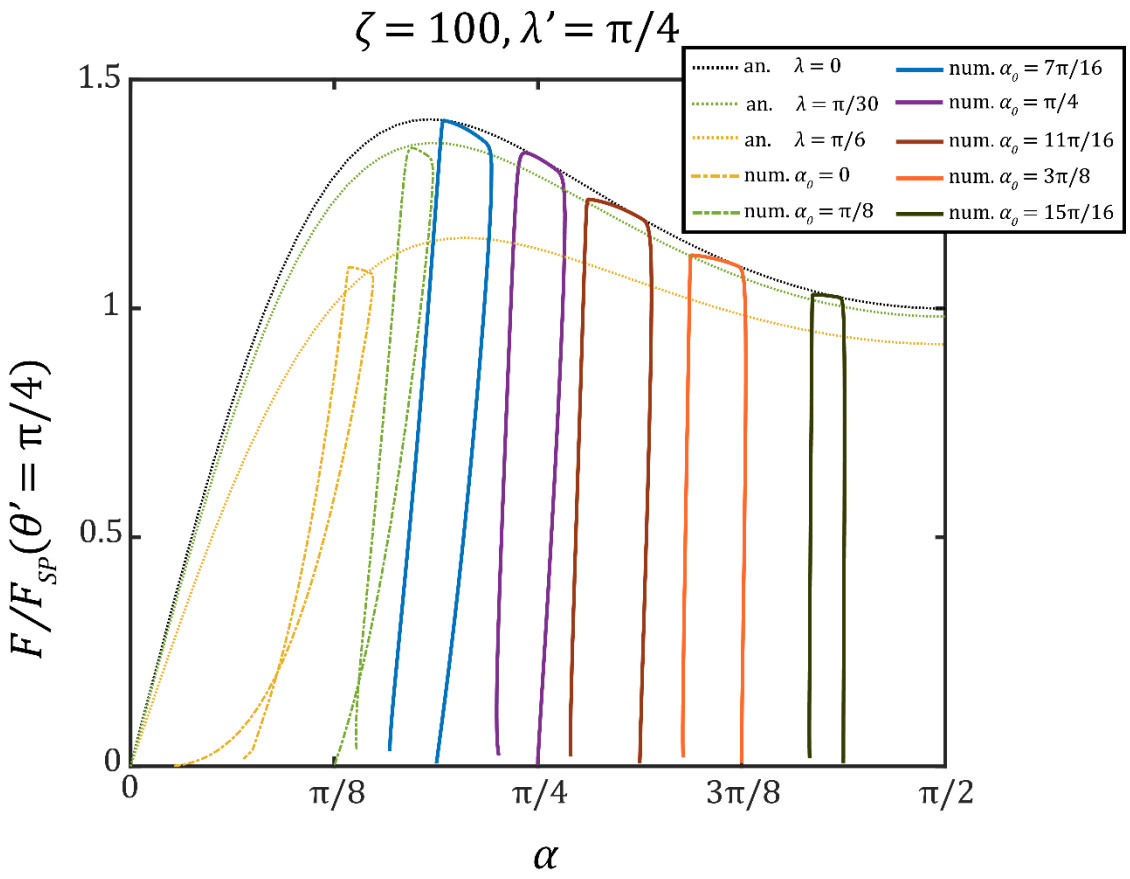

Figure S.II Normalized external force $F/F_{SP}(\theta' = \pi/4)$ vs α for different values of the initial value α_0 of the angle α. During the elastic phase λ and α evolve. When $F \geq F_P = F_P(\alpha, \theta, \lambda)$, α decreases following the analytical solution. The discrepancies between the numerical and analytical solutions are given by the variations of λ, as shown by including the analytical solutions for $\lambda = \pi/30$ and $\lambda = \pi/6$, which are the peak values of λ during the peeling phase for $\alpha_0 = \pi/8$ and $\alpha_0 = 0$. Higher variations of α, and thus of ϕ and λ, are observed for low values of α_0.

Adhesion of tapes with quadratic stress-strain laws

To evaluate the influence of the chosen linear elastic approximation in the numerical approach, we now consider a nonlinear constitutive law with stress hardening ($\sigma = E \cdot \varepsilon + C_1 E \cdot \varepsilon^2$), and evaluate the change in the peeling evolution of the attachment. Results are shown in Figure S.III. It is apparent that for relatively large values of the nonlinearity (the quadratic term up to 5 times the linear term), there is a limited effect on mechanical properties of the attachment. The effect of the nonlinearity is to generate a slightly less compliant attachment, with a higher detachment force and lower ultimate displacement.

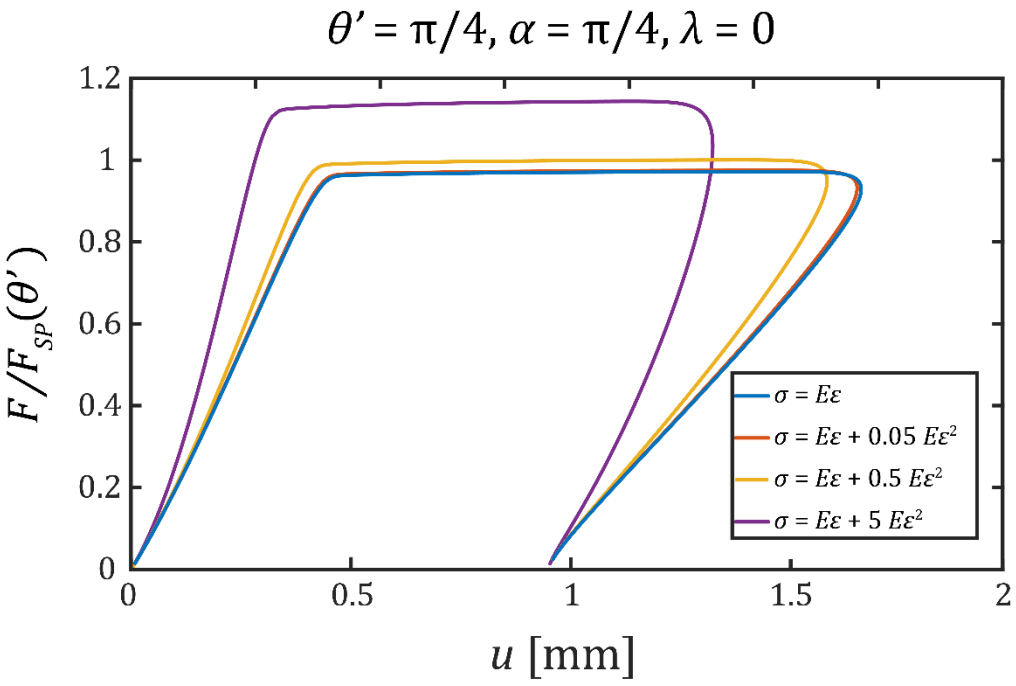

Figure S.III: Normalized applied force $F/F_{SP}(\theta')$ vs displacement for linear or nonlinear (stress hardening) constitutive laws for the tape material.**Strain evolution in the bilinear tape**

We observe the evolution of the strain levels of the bilinearly elastic structure described in Section 5 of the main manuscript. We consider the case $\lambda' = 2\pi/9$. The evolution of the peeling force and of the angles describing the structure are

described in Figure 13 of the main manuscript for both the numerical simulations and the experimental test. Due to the symmetries in the structure, we solely consider one of the two branches. We define $\mathrm{X} \in [0,1]$ as the tape relative coordinate, where $\mathrm{X} = 0$ identifies the edge of the tape attached to the hinge mechanism (see Figure 12 of the main manuscript) and $\mathrm{X} = 1$ identifies the opposite edge. The critical strain $\varepsilon_1 = 0.024$ is not reached by any point in the structure. Furthermore, once a point detaches completely from the substrate, its strain becomes independent from its original position, i.e. the strain in the detached trait of the branch is uniform. The observed nonlinear behaviour of the strain distribution during detachment is dependent from the traction-separation law used to describe the adhesive interface, as observed in (Brely et al., 2018).

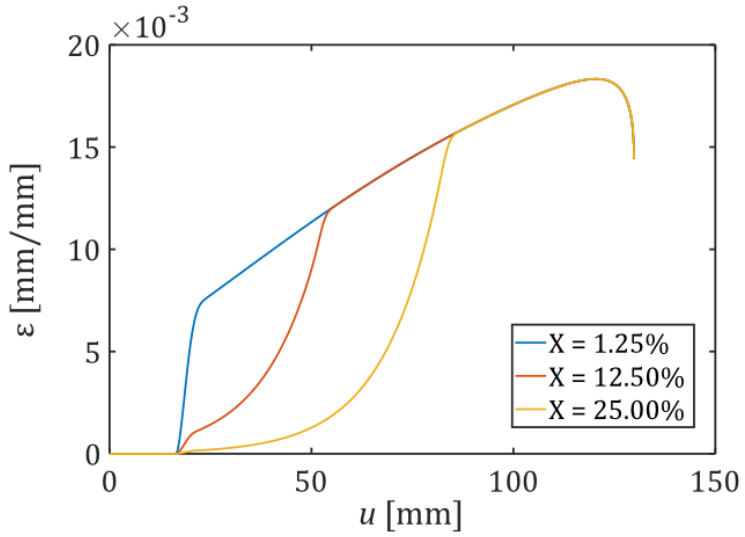

Figure S.IV: Strain vs displacement for three different points of one of the two tapes in the structure, identified by their relative position X.

References

Brely, L., Bosia, F., & Pugno, N. M. (2018). The influence of substrate roughness, patterning, curvature, and compliance in peeling problems. *Bioinspiration & Biomimetics*, *13*(2), 026004. https://doi.org/10.1088/1748-3190/aaa0e5